

**AJP**

ISSN : 0971 - 3093

Vol 26, No 2, February 2017

# ASIAN JOURNAL OF PHYSICS

**An International Research Journal**



**ANITA PUBLICATIONS**

FF-43, 1st Floor, Mangal Bazar, Laxmi Nagar, Delhi-110 092, India

B O : 2, Pasha Court, Williamsville, New York-14221-1776, USA



## Comparative analysis and implementation of a low cost, portable, and full field of view fringe projection profilometry imaging system

Anh Thai, Dat Tran, Thanh Nguyen, and George Nehmetallah\*

*EECS Department, The Catholic University of America,  
Washington DC 20064, USA*

In this work, an automated, portable, optimized, tabletop, low cost, and full field of view (FFOV) 3D scanning system based on fringe projection profilometry (FPP) using off-the-shelf components is constructed. A graphical user interface (GUI) to control, automate, and synchronize the whole FFOV-FPP system is developed. The constructed system is equipped with different recording and reconstruction capabilities depending on the user's constraints of accuracy, speed, and portability. A detailed comparative analysis and complete discussion of all the different steps of the recording and reconstruction process of the FFOV-FPP imaging system is conducted. Specifically, fringe analysis, phase error compensation methods, and spatial and temporal phase unwrapping is discussed in details. Two dimensional image registration is used to attach the real texture to the computed height profile and a 3D image fusion using an iterative closest point (ICP) algorithm for a FFOV reconstruction will also be developed as part of this work. Experimental results at each step of the process will be shown and the accuracy of the system is discussed. © Anita Publications. All rights reserved.

**Keywords:** Instrumentation measurement and Metrology, Three-dimensional sensing, Three-dimensional image acquisition, Fringe Projection, Structured lighting.

### 1 Introduction

Due to the fast and growing demand from the manufacturing industry (reverse engineering of prototypes) [1, 2], academia [3], medical industry (dental imaging, prosthetics, surgery, artificial organs, plastic surgery) [4], entertainment industry (3D photography and 3D movies) [5,6], fashion industry (3D body scanning and 3D printed clothing) [7], military (range finding, laser scanning for mines, surveillance) [8,9], surveying (3D topography) [10], and forensic science (3D face recognition, impressions on fired bullets, accident and crime scene reconstruction) [11], the last three decades have witnessed a plethora of research and new techniques to obtain high resolution, high speed, high dynamic range (depth), large field of view (FOV), portable, user friendly, and above all low cost 3D imaging techniques. Three dimensional imaging technologies can be classified depending on many criteria such as the methodology (triangulation, time delay, or monocular), active or passive, contact or noncontact, direct or indirect [12,13]. Fringe projection profilometry (FPP) technique discussed here is noncontact, active, direct, and based on triangulation [14]. All of these 3D technologies have advantages and disadvantages. FPP technique which is a subset of structured light technology has been an active area of research for three decades [14]. *State-of-the-Art* FPP systems have many advantages such as portability, high-speed, high-resolution, medium range, immunity to motion, compactness, large FOV, reliability in performance, and relatively low cost.

The proposed work has two motivations. Firstly, is to build a flexible, automated, portable, full field of view (FOV), and low cost FPP scanning system with off-the-shelf components: a portable projector, a portable CMOS camera, an Arduino microcontroller, and a stepper motor controlling a rotating stage. The system will be automated by a MATLAB® based GUI to control and synchronize the different components.

*Corresponding author :*

*e-mail:* [nehmetallah@cua.edu](mailto:nehmetallah@cua.edu) (George Nehmetallah)

Secondly, is to conduct a detailed comparative analysis of all the different steps of the recording and reconstruction process of the FFOV-FPP 3D imaging system. In this work, we emphasize on the fringe analysis, phase error compensation techniques, and spatial and temporal phase unwrapping. A texture will be attached to the height profile using 2D image registration and a 3D image fusion using an iterative closest point (ICP) algorithm for a FFOV reconstruction will also be implemented. The constructed FPP system will be equipped with different recording and reconstruction capabilities depending on the user's constraints of accuracy and speed. Experimental results are shown at each step of the process and the accuracy of the system is discussed.

## 2 Detailed description of the proposed FPP system: Calibration, recording, and reconstruction steps

The FPP optical setup is shown in Fig 1 (a) and the calibration, recording, and reconstruction steps are shown in Fig 1(b). In the first step, camera calibration aims at finding the intrinsic and extrinsic camera parameters and correcting the lens aberrations and distortions.

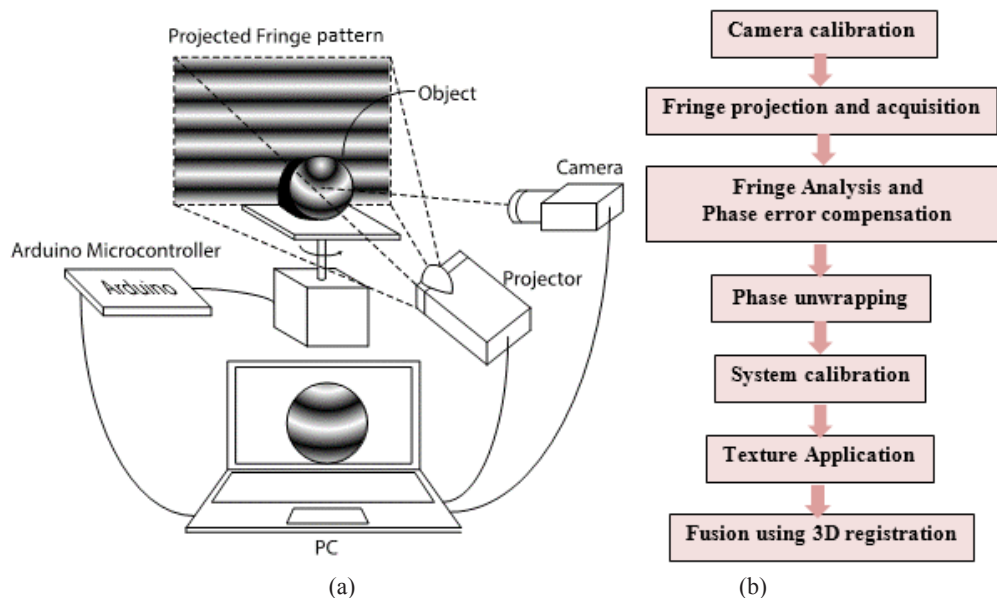


Fig 1. (a) Optical system setup. The off-the-shelf components: a projector, a CMOS camera, an Arduino board, a stepper motor and a rotating stage, a laptop running the GUI, and a cardboard screen behind the object, (b) Flow chart of the recording and reconstruction steps of the FPP system.

In the second step, sinusoidal fringe patterns with varying phase shift and frequency created by the developed GUI are projected on the object to be scanned at several angle of the stepper motor. The patterns that are modified by the object's topography are captured by the CMOS camera and relayed to the GUI for analysis. The rotation stage is driven by an Arduino board which is controlled by the GUI. The GUI ensures the synchronization between the captured images and the projected patterns. In the third step, the projector and CMOS camera nonlinearity are corrected by using phase error compensation, resulting in a wrapped phase map which is indirectly proportional to the object depth. Phase unwrapping is performed in the fourth step resulting in a phase map directly proportional to the object depth. System calibration performed in the fifth step converts the depth phase map in radians to real depth map in meters. Two-dimensional registration is performed in step number six to attach a texture to the height map. In the last step, 3D image registration using iterative closest point (ICP) algorithm is performed to obtain a full field-of-view 3D image. Complete details of each of these steps are described in the following subsections.

### 2.1 Estimation of the intrinsic, extrinsic, and nonlinear distortion camera parameters

As shown in Fig 2, the first step in any FPP technique is to perform camera calibration based on the pinhole model to estimate the intrinsic and extrinsic camera parameters. To obtain the extrinsic camera parameters, the rotation and translation coefficients that relate the real world coordinates to camera coordinates have to be determined. This is described as [15,16]:

$$\begin{pmatrix} x_c \\ y_c \\ z_c \end{pmatrix} = (\mathbf{R}, \mathbf{T}) \begin{pmatrix} x_w \\ y_w \\ z_w \end{pmatrix}, \begin{pmatrix} r_{11} & r_{12} & r_{13} & t_1 \\ r_{21} & r_{22} & r_{23} & t_2 \\ r_{31} & r_{32} & r_{33} & t_3 \end{pmatrix} \begin{pmatrix} x_w \\ y_w \\ z_w \\ 1 \end{pmatrix} \quad (1)$$

where  $(x_c, y_c, z_c)^T$  is the camera coordinate system of an arbitrary point,  $(x_w, y_w, z_w)^T$  is the corresponding real world coordinate system of that point, and  $\mathbf{T} = [t_i]^T$ ,  $\mathbf{R} = [r_{ij}]$  are the unknown translation and rotation matrices, respectively. The  $r_{ij}$  and the  $t_i$  parameters are the unknown extrinsic camera parameters. The transformation from camera coordinates  $(x_c, y_c, z_c)$  to camera pixel coordinates  $(u, v)$  is done according to the following equation:

$$z_c \begin{pmatrix} u \\ v \\ 1 \end{pmatrix} = \begin{pmatrix} \alpha & \beta & u_0 \\ 0 & \beta & v_0 \\ 0 & 0 & 1 \end{pmatrix} \begin{pmatrix} x_c \\ y_c \\ z_c \end{pmatrix} \quad (2)$$

where  $\alpha = f_u s_u$ ,  $\beta = f_v s_v$ ,  $f_u s_u$  are the horizontal and vertical focal lengths of the camera, respectively,  $s_u, s_v$  are scale factors,  $\gamma$  describes the skewness of the image axes, and  $u_0, v_0$  are the principal points of the camera. These parameters are the unknown intrinsic camera parameters.

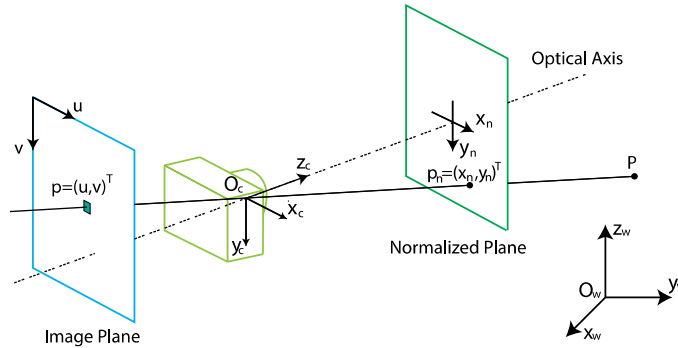


Fig 2. The linear camera model showing the labeling of the different axes of the lens and image plane of the camera [18].

The total transformation based on Eqs (1) and (2) becomes:

$$z_c \begin{pmatrix} u \\ v \\ 1 \end{pmatrix} = \begin{pmatrix} \alpha & \beta & u_0 \\ 0 & \beta & v_0 \\ 0 & 0 & 1 \end{pmatrix} \begin{pmatrix} r_{11} & r_{12} & r_{13} & t_1 \\ r_{21} & r_{22} & r_{23} & t_2 \\ r_{31} & r_{32} & r_{33} & t_3 \end{pmatrix} \begin{pmatrix} x_w \\ y_w \\ z_w \\ 1 \end{pmatrix} \quad (3)$$

The camera coordinate system  $(x_c, y_c, z_c)^T$  can be normalized to a transverse system  $(x_{cn}, y_{cn})^T$  as described in the following equation [17]:

$$\begin{pmatrix} u \\ v \\ 1 \end{pmatrix} = \begin{pmatrix} \alpha & \beta & u_0 \\ 0 & \beta & v_0 \\ 0 & 0 & 1 \end{pmatrix} \begin{pmatrix} x_c/z_c \\ y_c/z_c \\ 1 \end{pmatrix} = \begin{pmatrix} \alpha & \beta & u_0 \\ 0 & \beta & v_0 \\ 0 & 0 & 1 \end{pmatrix} \begin{pmatrix} x_{cn} \\ y_{cn} \\ 1 \end{pmatrix} \quad (4a)$$

Equation (4a) leads to the relation between the normalized camera transverse coordinate system and the real word coordinate system according to the following equation:

$$\begin{pmatrix} x_{cn} \\ y_{cn} \end{pmatrix} = \begin{pmatrix} r_{11} & r_{12} & r_{13} & t_1 \\ r_{21} & r_{22} & r_{23} & t_2 \end{pmatrix} \begin{pmatrix} x_w/S \\ y_w/S \\ z_w/S \\ 1 \end{pmatrix} \quad (4b)$$

where  $S = r_{31} x_w + r_{32} y_w + r_{33} z_w + t_3$

There are two types of distortions in the practical and simplified camera model: radial distortion and tangential distortion. These distortions can be described as [15,17]:

$$\delta_r = (k_1 r_{cn}^2 + k_2 r_{cn}^4) \begin{pmatrix} x_{cn} \\ y_{cn} \end{pmatrix} \begin{bmatrix} (k_1 r_{cn}^2 + k_2 r_{cn}^4) x_{cn} \\ (k_1 r_{cn}^2 + k_2 r_{cn}^4) y_{cn} \end{bmatrix} \quad (5a)$$

$$\delta_t = \begin{bmatrix} 2k_3 x_{cn} y_{cn} + k_4 (2x_{cn}^2 + r_{cn}^2) \\ k_3 (2y_{cn}^2 + r_{cn}^2) + 2k_4 x_{cn} y_{cn} \end{bmatrix} \quad (5b)$$

Where  $\delta_r$  and  $\delta_t$  are the radial distortion and tangential distortion, respectively,  $k_1$ ,  $k_2$ ,  $k_3$ , and  $k_4$ , are the distortion coefficients, and  $r_{cn} = \sqrt{x_{cn}^2 + y_{cn}^2}$  is the normalized radial distance. Therefore, the normalized camera transvers coordinates system after accounting for distortion is described as

$$\begin{pmatrix} x_d \\ y_d \end{pmatrix} = \begin{pmatrix} x_{cn} \\ y_{cn} \end{pmatrix} + \delta_r + \delta_t = \begin{bmatrix} x_{cn}(1 + k_1 r_{cn}^2 + k_2 r_{cn}^4) + 2k_3 x_{cn} y_{cn} + k_4 (2x_{cn}^2 + r_{cn}^2) \\ y_{cn}(1 + k_1 r_{cn}^2 + k_2 r_{cn}^4) + k_3 (2y_{cn}^2 + r_{cn}^2) + 2k_4 x_{cn} y_{cn} \end{bmatrix} \quad (6)$$

Accounting for lens distortion, and according to Eq (4a), the modified pixel coordinates off the camera are related to the normalized camera transvers coordinates by the following equation

$$\begin{pmatrix} u_d \\ v_d \\ 1 \end{pmatrix} = \begin{pmatrix} \alpha & \beta & u_0 \\ 0 & \beta & v_0 \\ 0 & 0 & 1 \end{pmatrix} \begin{pmatrix} x_d \\ y_d \\ 1 \end{pmatrix} \quad (7)$$

The lens distortion model discussed above causes significant distortion in the pixels located far away from the principal points and leads to incorrect unwrapped phase retrieval if not compensated for. The camera calibration problem can be solved by using images of a checkerboard with different orientations and having pre-determined sizes. Since the size of each square of the checkerboard is known, capturing the images provides experimental camera coordinates:  $(u_{d, exp}, v_{d, exp})$  and  $(x_w, y_w, z_w)$ . The intrinsic, extrinsic, and distortion coefficients can be estimated by nonlinearly minimizing the following function using Levenberg-Marquardt algorithm:

$$\min_{(k_1, k_2, k_3, k_4, \alpha, \beta, \gamma, u_0, v_0, r_{kl}, t_1, 2, 3)} \sum_{i=1}^M \sum_{j=1}^N [(u_d - u_{d, exp})^2 + (v_d - v_{d, exp})^2] \quad (8)$$

The initial guess for the camera parameters can be obtained by neglecting the nonlinear parameters using Eq (3) (See Appendix a for complete derivation).

## 2.2 Fringe projection and acquisition method

In the FPP system discussed in this paper, sinusoidal fringes with varying frequencies and phase shifts are generated using a MATLAB® based GUI and then projected using a DLP projector to a screen behind the test object (See Fig 1 (a)). A CMOS camera is used to capture the deformed sinusoidal fringes due to the test object's structure. In the proposed setup, the projected fringe patterns' parameters such as, field of view, number of phase shifts, pitch, and angle, can be controlled by the developed GUI. These parameters affect the speed, the resolution, and the size of the reconstructed 3D object. While other types of fringe patterns like the binary coding pattern are robust to noise [19] and do not suffer from nonlinear effects of the projector and the camera, sinusoidal patterns are better in terms of high-resolution measurements. To

obtain high accuracy in the 3D reconstruction while maintaining high-speed measurement, sinusoidal fringe patterns with nonlinear intensity correction is adopted. The initial generated intensity  $I_{0n}$  at the  $(x, y)$  pixel coordinates of the  $n^{th}$  phase shifted sinusoidal fringe pattern before nonlinear correction can be described as [20]:

$$I_{0n}(x, y) = I_m \left\{ 1 + \cos \left[ 2\pi f \left( \frac{x \cos(\alpha)}{W} \right) + \left( \frac{y \sin(\alpha)}{H} \right) + \delta_n \right] \right\}, \quad (9)$$

where  $I_m$  is the intensity modulation amplitude,  $f$  is the frequency of the pattern,  $\delta_n = 2\pi(n-1)/N$  is the  $n^{th}$  phase shift with  $N$  is the maximum number of phase-shift steps (minimum number is 3),  $\alpha$  is the angle of the fringe patterns, and  $W$  and  $H$  are the width and height of the fringe patterns, respectively. Since both the camera and projector introduce nonlinear luminance distortion, the captured intensity can be written as

$$I_{cn}(u, v) = a(u, v) + \sum_{m=1}^M b_m(u, v) \cos \{m[\varphi^w(u, v) + \delta_n]\}, \quad (10)$$

where  $I_{cn}(u, v)$  is the captured intensity of the  $n^{th}$  fringe pattern using camera coordinate,  $\varphi^w$  is the wrapped phase to be computed,  $a(u, v)$  is the background intensity, and  $b_m(u, v)$  is the intensity modulation of the  $m^{th}$  order harmonic which is due to the nonlinearity of the camera and projector. Starting with a generated fringe pattern intensity  $I_0$  as described in Eq (9), the captured intensity due to nonlinearity of the system is  $I_c$  as shown in the block diagram in Fig 3, where  $f_p$  and  $f_c$  denote the transfer functions of the projector and the camera, respectively. As shown in Eq (10), the nonlinearity is described by the higher order harmonics which can be mitigated by increasing the number of phase-shifting steps:  $N \geq (M + 2)$ . Figure 4 shows a typical nonlinear response function  $f = f_c(f_p(\cdot))$  of the system. Section 2.3 describes the phase error compensation mechanism adopted for the developed FPP system.

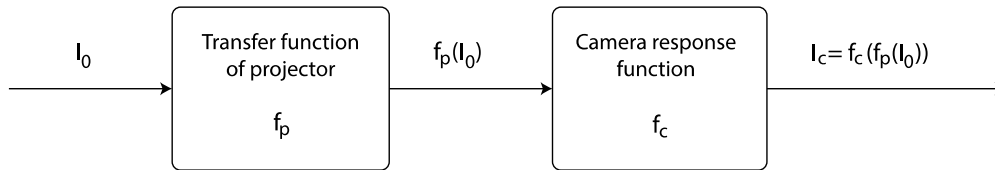


Fig 3. Block diagram describing the relation between the intensity of the projected and captured fringe patterns due to the nonlinear luminance distortion caused by the projector and camera.

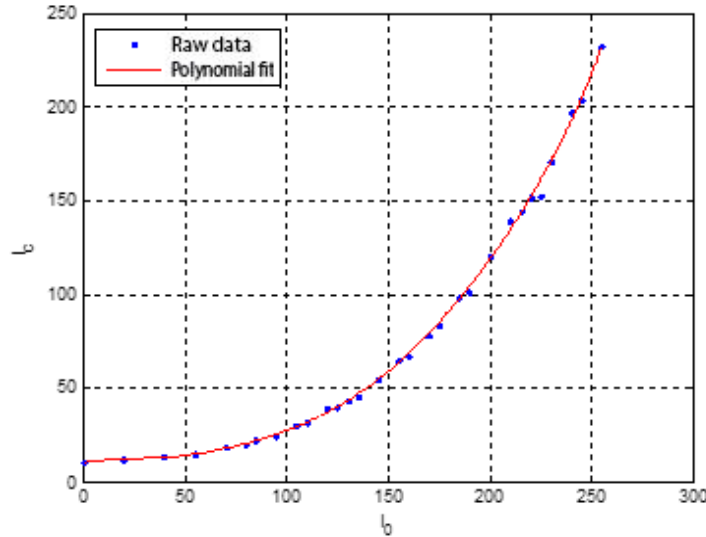


Fig 4. Typical nonlinear response function:  $f = f_c(f_p(\cdot))$  of the system.

### 2.3 Fringe analysis and phase error compensation methods

Different approaches have been developed to retrieve full-field wrapped phase distribution for FPP systems. These approaches are mainly divided into two categories: (a) Transform based schemes and (b) phase shifting based schemes. The former uses different transforms such as wavelet transform or Hilbert transform to overcome the nonlinear distortion of the system; however, they lack the ability to measure objects with complex shapes or multiple objects at the same time [21]. The latter category is based on phase shifting and has the ability to measure multiple objects with complex shapes with a reduced computational cost [20]. In this paper, the wrapped phase is obtained from the fringe patterns using a combination of phase shifting and phase-error compensation technique. There is always a trade-off between high accuracy and computational cost (high-speed measurement) using this combined technique. A generalized full-field phase retrieval can be described as [20]:

$$\varphi^w(u, v) = \arctan \frac{-\sum_{n=1}^N \sin(\delta_n) I_{cn}(u, v)}{\sum_{n=1}^N \cos(\delta_n) I_{cn}(u, v)}, \quad (11a)$$

where  $I_{cn}(u, v)$  is the captured intensity of the  $n^{\text{th}}$  fringe pattern using camera coordinate,  $\varphi^w$  is the unknown wrapped phase. Since  $\varphi^w$  is distorted by the nonlinear response of the CCD and projector a phase-error compensation method is necessary to compensate for this nonlinearity. For the case of  $N = 3$  intensity patterns, Eq (11a) can be written as

$$\varphi^w(u, v) = \arctan \frac{\sqrt{3} (I_{c1}(u, v) - I_{c3}(u, v))}{2I_{c2}(u, v) - I_{c1}(u, v) - I_{c3}(u, v)}, \quad (11b)$$

As for phase error compensation, a phase error look-up table (LUT) compensation method to enhance the accuracy of the system was proposed in Ref [22]. While this method is simple to implement by directly analyzing the captured image of a flat board, it only gives accurate results when the pitch of the pattern is large enough. Also, this method is not compatible with multiple frequency phase-shifting method, making the system unsuitable of measuring multiple complex shape objects. Moreover, this method is sensitive to the configuration and measurement conditions of the system [20]. Other approaches use gamma correction to compensate for the nonlinear effect. The nonlinearity of the projector is roughly a power function of gamma coefficient which can be described as [21].

$$I_{ci} = aI_{oi}^\gamma + b \quad (12)$$

where  $I_{ci}$  is the output at the  $i^{\text{th}}$  grayscale intensity value for a given grayscale input value  $I_{oi}$ ,  $a$  and  $b$  are constants, and  $\gamma$  is the unknown constant to be estimated using least squares method, statistical methods, or directly by comparing with the ideal phase map to analyze the phase error [21]. Many researchers introduced different gamma estimation strategies for structured light 3D based system where the gamma value is estimated based on a specific pitch pattern [20]. In these techniques, the phase error is compensated by applying an inverse gamma function to the input fringe patterns ( $I_{mi} = I_{oi}^\gamma \Rightarrow I_{oi} = I_{mi}^\gamma$ ) before being projected onto the object, where  $I_{mi}$  stands for the modified input  $i^{\text{th}}$  grayscale intensity of the fringe pattern.

However, with the development of the image enhancing circuitry in various projectors nowadays, the gamma model described in Eq (12) is not valid anymore. In this study, the system is modeled using a polynomial of order  $P$  which describes the relationship between generated intensity and captured intensity which can be written as [21]

$$I_{ci} = \sum_{k=0}^P c_k I_{oi}^k, \quad (13)$$

where  $c_k = \{1, 2, 3\}$  are coefficients to be calculated and  $I_{ci}$  are the captured images. In this method, the initial intensity fringe patterns are predistorted before projection. Hence, the inverse function to Eq (13) can be fitted as

$$I_{oi} = \sum_{k=0}^P a_k I_{ci}^k \quad (14)$$

where  $a_k = \{1, 2, 3\}$  are the unknown coefficients of the polynomial of order  $P$ . Let  $I_{mi}$  be the modified projected input intensity pattern for a desired captured intensity pattern:  $\hat{I}_{0i}$

The objective is to recover the sinusoidal fringe pattern by finding the inverse of the transfer function of the system  $f = f_c (f_p (\cdot))$  as illustrated in Fig 5.

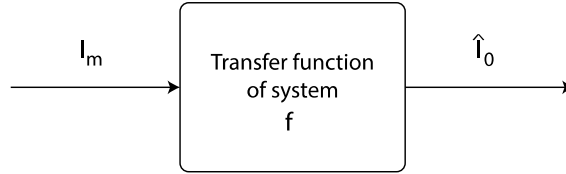


Fig 5. Phase-error compensation block diagram relating modified input to the desired captured fringe patterns

Thus, a sequence of  $L - l + 1$  uniform grayscale intensity images  $I_{mi}$  are projected on a flat screen. To avoid saturation, the grayscale intensities range between  $I = [l, L]$ , which is in the linear region of the projector. The  $i^{\text{th}}$  image captured by the camera is labeled:  $\hat{I}_{0i}$ . The modified  $i^{\text{th}}$  projected input grayscale intensity image can then be written as

$$I_{mi} = \sum_{k=0}^P a_k \overline{\hat{I}_{0i}^k} \tag{15a}$$

where  $\overline{\hat{I}_{0i}^k}$  is the average of the  $k^{\text{th}}$  power of the  $i^{\text{th}}$  grayscale captured image. In matrix notation this can be rewritten as

$$I_m = \hat{I}_0 a \tag{15b}$$

where  $\hat{I}_0$  is an  $(L - l + 1 \times P + 1)$  matrix containing the average of the  $k^{\text{th}}$  power of all the grayscale captured images,  $a$  is an  $(8 \times 1)$ ,  $I_m$  is an  $(L - l + 1 \times 1)$  vector containing the estimate of the modified projected images. Equation (15b) can be written as:

$$\begin{bmatrix} 1 & \overline{\hat{I}_{0l}} & \overline{\hat{I}_{0l}^2} & \overline{\hat{I}_{0l}^3} & \overline{\hat{I}_{0l}^4} & \overline{\hat{I}_{0l}^5} & \dots & \overline{\hat{I}_{0l}^P} \\ \vdots & \vdots \\ 1 & \overline{\hat{I}_{0i}} & \overline{\hat{I}_{0i}^2} & \overline{\hat{I}_{0i}^3} & \overline{\hat{I}_{0i}^4} & \overline{\hat{I}_{0i}^5} & \dots & \overline{\hat{I}_{0i}^P} \\ \vdots & \vdots \\ 1 & \overline{\hat{I}_{0L}} & \overline{\hat{I}_{0L}^2} & \overline{\hat{I}_{0L}^3} & \overline{\hat{I}_{0L}^4} & \overline{\hat{I}_{0L}^5} & \dots & \overline{\hat{I}_{0L}^P} \end{bmatrix} \begin{bmatrix} a_0 \\ a_1 \\ a_2 \\ a_3 \\ a_4 \\ a_5 \\ \vdots \\ a_P \end{bmatrix} = \begin{bmatrix} I_{ml} \\ I_{ml+1} \\ \vdots \\ I_{mi} \\ \vdots \\ I_{mL-1} \\ I_{mL} \end{bmatrix} \tag{15c}$$

Equation (15) is an over determined least squares problem and can be solved by minimizing the least square error of the objective function:

$$\min_a \{S\} = \min_a \{ \sum_{i=1}^{L-l+1} [ \sum_{k=0}^P a_k \overline{\hat{I}_{0i}^k} - I_{mi} ]^2 \}, \tag{16}$$

where the unknown coefficients  $a_k$  are estimated by minimizing the least square error by solving:  $\partial s / \partial a_k = 0, \forall k$ . Figure 6 shows the experimental nonlinear gamma error compensation curve of the system using polynomial fitting where  $P = 7$ .

This gamma correction technique was applied to the system and the periodic phase error was significantly reduced. The wrapped phase map is then estimated by the following equation [20]:

$$\hat{\phi}^v(u, v) = \arctan \frac{-\sum_{n=1}^N \sin(\delta_n) \hat{I}_0(u, v)}{\sum_{n=1}^N \cos(\delta_n) \hat{I}_0(u, v)}, \tag{17}$$

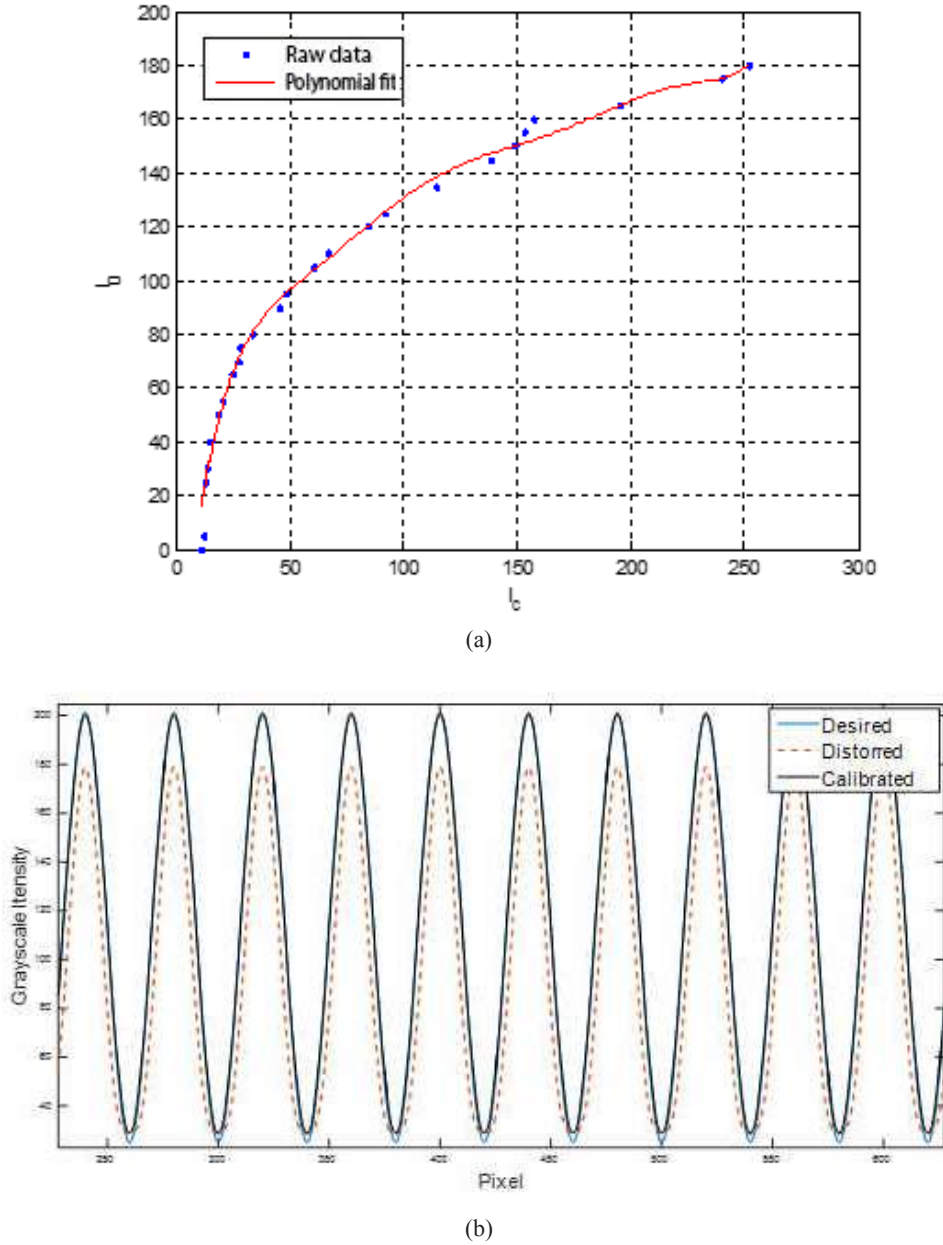


Fig 6. Nonlinear gamma error compensation curve using polynomial fitting where  $P = 7$ . (a) Nonlinear gamma curve (blue squares) and fitted polynomial curve (solid red line); (b) Desired (solid blue line), distorted (dashed red line), and calibrated (solid black line) sinusoidal wave with nonlinear polynomial correction.

#### 2.4 Spatial and temporal phase unwrapping techniques

In the previous section, the wrapped phase  $\hat{\phi}^w(u, v)$  with  $2\pi$  ambiguity was computed. In order to evaluate the absolute phase height of the scanned object, the wrapped phase must be converted to continuous phase through an unwrapping process. Phase unwrapping techniques can be divided into two main categories (a) spatial unwrapping and (b) temporal unwrapping [23]. Spatial unwrapping techniques

perform well with relatively smooth surfaces but often lack high accuracy with surfaces that have sharp step-height variations with multiple objects which need special hierarchical unwrapping algorithms [24]. On the other hand, temporal unwrapping techniques perform well with complex shapes and with the presence of isolated areas with sharp step-height variations. However, this high accuracy of temporal techniques need high processing speed because of the requirement of using multiple frequency with multiple phase shifting steps to retrieve the unwrapped phase of the object. Both of these techniques are briefly discussed in this work and can be selected in the developed GUI depending on the application requirements.

#### 2.4.1 Spatial phase unwrapping techniques

Spatial phase unwrapping is used to decipher wrapped phase maps computed by the *arctan* function which are in the interval between  $-\pi$  and  $\pi$  in order to derive the absolute phase, or equivalently, the depth information. Spatial unwrapping techniques require only one single wrapped phase which make them suitable in high-speed 3D reconstruction. Many techniques have been proposed for this purpose [24]. Most of these techniques compute the measured gradient of the phase field, which is subsequently integrated to recover the unwrapped phase. One of the earliest approaches is the residue identification and cuts to limit the possible integration paths [25], while another class of approaches use least-squares techniques [26]. The techniques that rely on the residue-cut algorithms are quite accurate but do not produce good estimates in regions of moderate phase noise [27]. The least-squares methods yield complete coverage of the phase but at the cost of distortion in the recovered phase field. Another synthesis approach, combining the two approaches, offers greater spatial coverage with less distortion in many instances [27]. In FPP 3D based systems, the quality of the measurement is based on the frequency of the projected fringe pattern. By using spatial phase unwrapping method, one wrapped phase measurement of high frequency fringe pattern (i.e. 8 pixels per fringe) is enough to unwrap the phase map.

In this Section, we implemented a fast 2D unwrapping method based on reliability function that does not follow a continuous path [28]. The unwrapped phase obtained, contain both information about the object's phase (shape) and carrier-frequency related phase [29]. Reference-subtraction, which is based on measuring the object and the reference separately, is one of the techniques used to eliminate the phase due to the carrier-frequency. The phase that corresponds to the object's shape is obtained by digitally subtracting unwrapped phase of the reference plane from the unwrapped phase of the object. The equation to acquire the phase that corresponds to the object's shape can be described as

$$\varphi_0^{uw}(u, v) = \varphi_{(0, r)}^{uw}(u, v) - \varphi_r^{uw}(u, v) \quad (18)$$

where  $u$  and  $v$  are the position in pixels in the image plane,  $\varphi_0^{uw}$  holds the information about the unwrapped phase related to the object's shape alone,  $\varphi_{(0, r)}^{uw}$  is the unwrapped phase of the object with the background tilt and  $\varphi_r^{uw}$  is the unwrapped phase of the reference plane (tilt due to carrier). This method is easy to implement and it works very well in removing linear and nonlinear carrier phases. The drawbacks of this method are that two separate measurements are needed hence is not suitable for high-speed systems and the phase measurement uncertainty is magnified as shown in the following equation [30]:

$$\varphi_{(0, r)}^{uw}(u, v) = \varphi_s(u, v) + \varphi_c(u, v) + \varphi_e(u, v) \quad (19a)$$

$$\varphi_r^{uw}(u, v) = \varphi_c(u, v) \pm \varphi_e(u, v), \quad (19b)$$

where,  $\varphi_s$ ,  $\varphi_c$  and  $\varphi_e$  are object shape-related phase, carrier phase, and phase error, respectively. Consequently, the overall uncertainty is increased over the phase map and Eq (18) becomes

$$\varphi_0^{uw}(u, v) = \varphi_{(0, r)}^{uw}(u, v) - \varphi_r^{uw}(u, v) = \varphi_s(u, v) \pm 2 \varphi_e(u, v) \quad (20)$$

The technique implemented in this paper is based on polynomial fitting of the carrier. The phase

due to the carrier can be approximated as a biquadratic polynomial

$$\varphi_c(u, v) = a_1 + a_2u + a_3v + a_4uv + a_5u^2 + a_6v^2, \quad (21)$$

where the unknown  $a_k$  parameters are obtained by minimizing the least square error:

$$\min_a \{E\} = \min_a \left\{ \sum_{m=1}^M [\varphi_{c,p}(u, v) - \varphi_c(u, v)]^2 \right\}, \quad (22)$$

where the phase data  $\varphi_{c,p}$  are chosen from the flat regions where there is no object. The error function  $E$  is minimized using  $M$  data points, and the unknown  $a_k$  parameters can be estimated accurately. Experimental results are discussed in Section 3.1.

#### 2.4.2 Temporal phase unwrapping techniques

Temporal phase unwrapping techniques are often used to acquire the 3D phase of complex shaped objects having isolated areas and sharp-height variations with high accuracy. Several sets of phase-shifted fringes having different frequencies (pitch) are needed to retrieve the fully unwrapped phase in a multi-phase shift multi-frequency iterative temporal phase unwrapping technique. In this technique, the pitch of each set of shifted fringe patterns varies over time; hence, the name temporal phase unwrapping. The initial (1<sup>st</sup> set) pitch is chosen in such a way to display a single fringe period covering the entire scanned object, to provide a continuous phase map, and to compute integer offset for higher order frequencies. At each  $i^{\text{th}}$  step (fringe pattern's frequency  $f_i$ ), the unwrapped phase map depends on the  $(i-1)^{\text{th}}$  unwrapped phase map and the  $i^{\text{th}}$  wrapped phase map which was obtained from Eq (17). The multi-phase shift multi-frequency iterative temporal phase unwrapping technique can be expressed as [31]

$$\varphi_i^{\text{uw}}(u, v) = \varphi_i^{\text{w}}(u, v) + 2\pi \times \text{round} \left( \frac{(k \times \varphi_{i-1}^{\text{uw}}(u, v) - \varphi_i^{\text{w}}(u, v))}{2\pi} \right), \text{ for } i = 2, 3, \dots, n \quad (23)$$

where  $\text{round}$  is the rounding operator to the nearest integer and  $k = f_i / f_{i-1}$  is the ratio between two adjacent frequencies ( $k \sim 3$  for high accuracy). The simplicity of Eq (23) reduces the computational cost of the reconstruction process. It is worth noting that the higher the  $n$  is, the higher the accuracy is at the expense of more computational processing. Hence, a trade-off between computational complexity and speed exist using this technique.

### 2.5 System Calibration

System calibration is a necessary step to extract the real height profile of the scanned object from the unwrapped phase map obtained in Eq (23). This step involves determining the actual lateral dimensions of the object using the camera calibration parameters obtained in Section 2.1. Generally speaking, there are two main approaches of unwrapped phase to real height profile conversion. The first approach converts the unwrapped phase to height directly using a specific system setup, while the second one performs phase to height conversion for an arbitrary setup. Both of these approaches are discussed here and the comparison between their performances is determined experimentally.

#### 2.5.1. Phase to height conversion using a specific system setup

Using a specific system setup as shown in Fig 7, a quick and easy calibration step can be conducted to establish the relationship between height of the object and its phase map. Since the CCD is parallel to reference plane there is a direct proportionality relationship between the phase map and the object's surface height which can be described as [18]

$$z(u, v) = K^{\text{uw}}(u, v) \quad (24)$$

where  $K$  is a constant. This constant can be crudely computed using  $= pl/2\pi d$ , where  $p$  is the fringe pitch on the reference plane, and  $d$  and  $l$  are the distances between the projector and CCD and the distance between CCD and the reference plane, respectively as shown in Fig 7. A more precise method to estimate the  $K$  parameter is through mounting multiple known-height gauge blocks attached to the reference plane. The linear-least square error between the phase map and the object's surface height can be defined as

$$S = \sum_{m=1}^M [K\phi^{uv}(u, v) - z(u, v)]^2, \quad (25)$$

where  $M$  is the number of data points and  $z(u, v)$  is the height at the point of transverse coordinates  $(u, v)$ . This method is limited by these conditions: (a) the reference plane must be exactly parallel to the CCD and/or the projector which is difficult to insure in practical laboratory conditions, (b) the projected fringe patterns must be distributed uniformly on the reference plane, and (c) the distortion due to the optical devices (lenses) or sensor noise is considered very small.

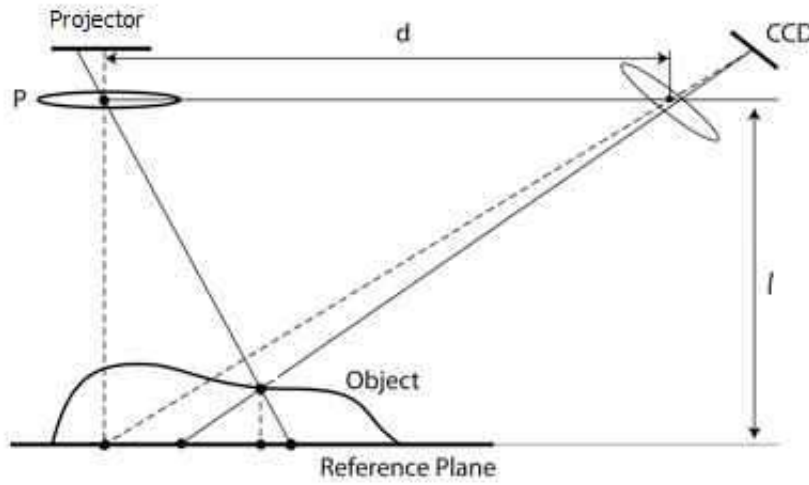


Fig 7. Phase-to-height conversion using a specific system setup [18].

### 2.5.2 Phase to height conversion using arbitrary system setup

For an arbitrary camera-projector setup shown in Fig 8, a generalization of Eq (24) needs to be derived. A more general biquadratic phase to out-of-plane height conversion relation for an arbitrary setup can be described as [32]:

$$z(u, v) = f_c / f_d, \quad (26)$$

where,  $f_c = \sum_{i=1}^{17} (c_i + c_{i+1} \phi^{uv}) u^k v^l$ ,  $f_d = \sum_{i=1}^{17} (d_i + d_{i+1} \phi^{uv}) u^k v^l$ ,  $k, l = 0, 1, 2$ , and  $\phi^{uv}$  is the unwrapped phase computed by Eq (23),  $u, v$  are camera pixel coordinates defined in Eq (2), and the  $c_i, d_i$  parameters can be determined by performing the non-linear least square error defined as [32]

$$S = \sum_{m=1}^M [z(u, v) - z_m(u, v)]^2, \quad (27)$$

where  $M$  is the total number of data points and  $z_m(u, v)$  is the height at each point  $(u, v)$ . The least squares criteria requires,  $\partial s / \partial c_i = \partial s / \partial d_j = 0$ , for  $i, j = 1, \dots, 17$ .

It is important to note that the coefficients are solved using nonlinear iterative techniques, and without good initial conditions (values), non-linear approaches usually get trapped in local minima and yield inaccurate results. The least square solution used to find the initial values of the coefficients, to be

later used in Eq (27), can be calculated using a linearized version of Eq (27).

$$S = \sum_{m=1}^M [f_c - f_d z_m(u, v)]^2. \quad (28)$$

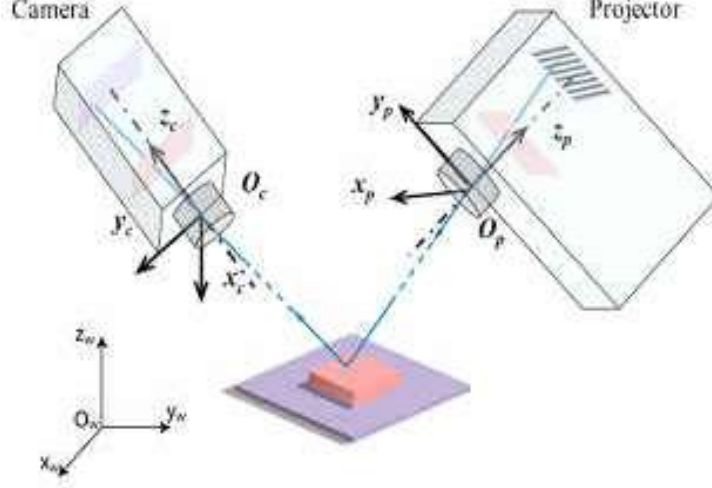


Fig 8. 3 D schematic illustration of a generalized FPP setup showing all labeled coordinates [18].

It is worth noting that this equation converts directly the unwrapped phase of the object to out-of-plane height. To account for the presence of the distortion of optical devices, the equation also includes second order terms to enhance the accuracy of the system. Because this method relies directly on the unwrapped phase of the object, it does not require carrier removal step or reference plane subtraction in real measurement.

### 2.5.3 Phase to real world coordinate conversion

The last step in the calibration process is to use the computed out-of-plane height profile of the object's surface in Eq (27) to compute the in-plane real world lateral coordinates  $x$  and  $y$  using the following equations [17]

$$x(u, v) = p_1(u, v) + p_2(u, v) \times z(u, v) \quad (29a)$$

$$y(u, v) = p_3(u, v) + p_4(u, v) \times z(u, v) \quad (29b)$$

$$\begin{aligned} \{p_1(u, v) = f_1(r_{ij}, t_{ij}) \text{ and } p_2(u, v) = f_2(r_{ij}, t_{ij}) \\ \{p_3(u, v) = f_3(r_{ij}, t_{ij}) \text{ and } p_4(u, v) = f_4(r_{ij}, t_{ij}) \end{aligned} \quad (29c)$$

where  $p_1, p_2, p_3,$  and  $p_4,$  are constants at each pixel, and  $f_{1, 2, 3, 4}$  are functions of the rotation and translation coefficients (See Appendix B) [17]. Equations (29a-c) show that the real world lateral coordinates  $x(u, v)$  and  $y(u, v)$ , depend on the computed height variable  $z(u, v)$ . Hence, the accuracy of  $x$  and  $y$  depends on the accuracy of the computed out-of-plane height profile of the object at that pixel.

## 3 Experimental setup and results of the portable FPP system with off-the-shelf components

Figure 9 shows the laboratory system set up. A calibration board and several calibration cubes with different sizes were custom fabricated and used for the calibration of the 3D FPP scanning system. The camera used in the experiments is a DFK 42BUC03 camera with 8-bit dynamic range. All the experimental results obtained are based on this configuration. The optical devices are arranged based on the triangulation theory. The contrast and brightness levels of the projector are adjusted in order to maximize the monotonic

region of the intensity transfer function, as discussed in details in Section 2.3.

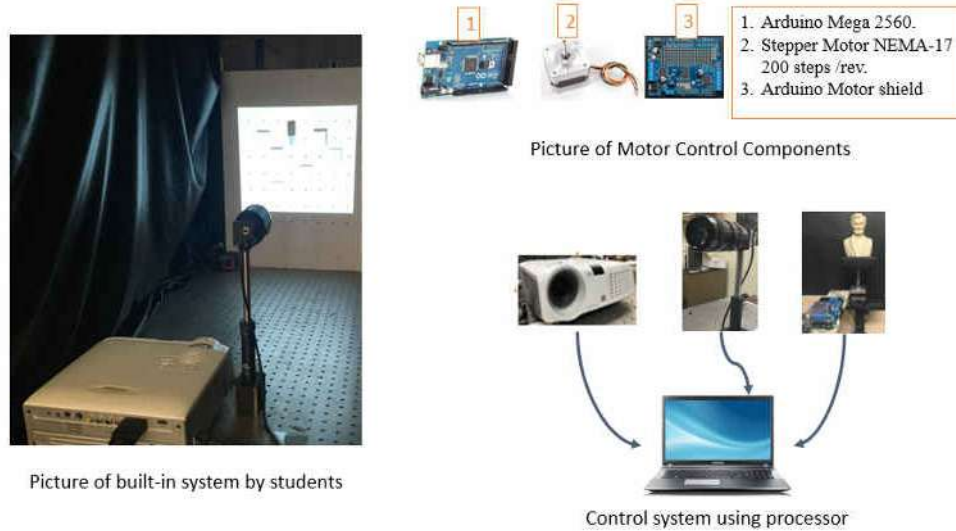


Fig 9. A simple 3D scanning system.

### 3.1 3D Reconstruction using a specific system setup and spatial unwrapping

In this first set of experiments, the unwrapped phase is obtained by using spatial unwrapping method and the non-linear carrier removal method as discussed in Section 2.4.1 to obtain the unwrapped phase map. Figure 10(a) shows the real 2D image of “President Lincoln” test object, Fig 10(b) shows the 3D point cloud height profile without texture, and Fig 10(c) shows the 3D point cloud height profile with texture. Using Eq (22), the carrier phase is estimated by surface-fitting of the region where actual object height is close to zero. The constant  $K$  from Eq (24) is pre-determined by using several precision known-height gauge blocks. Fig 11 is similar to Fig 10 but the “Lion Statue” test object is used.

In practical measurement, it is difficult to satisfy all of the conditions of this method. Therefore, some noise still remains in the reconstructed 3D image since the height of the reference plane is not uniform due to shadow noise. We also noticed that spatial unwrapping method fails to measure multiple complex objects with large and sharp height variation at the same time without phase ambiguity. Hence, the accuracy of this method is lower than the temporal phase unwrapping technique discussed in the following section.

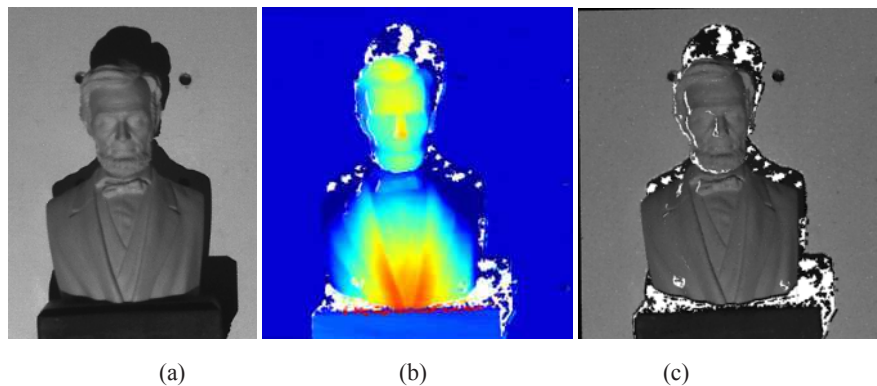
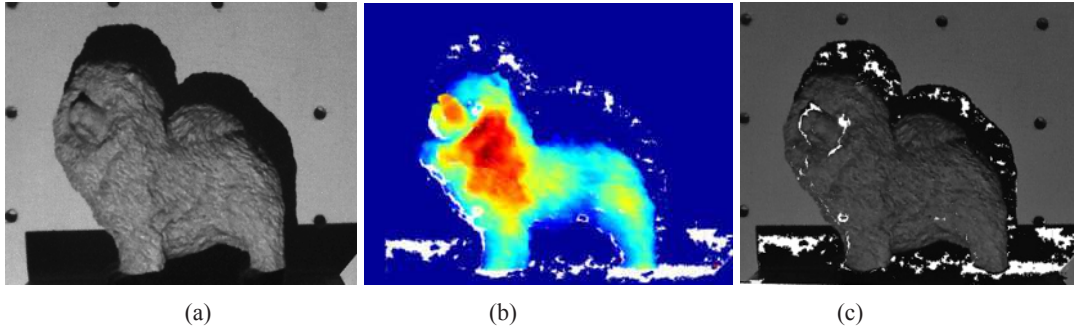


Fig 10. (a) Real 2D image of the test object; (b) 3D point cloud height profile without texture; (c) 3D point cloud height profile with texture.



**Fig 11.** (a) Real 2D image of the test object; (b) 3D point cloud height profile without texture; (c) 3D point cloud height profile with texture.

### 3.2. 3D Reconstruction using multiple frequencies and temporal phase unwrapping

In the second set of experiments, the unwrapped phase is obtained by using multi-frequency phase unwrapping algorithm as discussed in Section 2.4.2. A study relating the depth-variation sensitivity to the direction of the fringes was performed and horizontal fringes rendered the best results. As mentioned in Section 2.4.2, fringe patterns with multiple frequencies were used to reduce the noise influence on the results which lead to high accuracy for the unwrapped-phase distribution. Also in order to achieve high accuracy, and as mentioned in Sections 2.1 and 2.3, lens and gamma distortion have been reduced significantly before computing the unwrapped phase of the object. In order to verify the performance of the FPP system, different complex shape objects have been used. A set of five fringe patterns (1, 4, 16, 64, and 128), a ten-step phase shifting algorithm, lens distortion, and gamma correction have been used in these experiments. All the necessary reconstruction coefficients are estimated by using the techniques described in Section 2. Seven gauge blocks with different heights have been used in the calibration process. Holes were drilled on the top surfaces of the gauge blocks are used to verify the accuracy of the algorithm. The height precision for a set of 4 frequencies was determined to be  $200\ \mu\text{m}$ . Other experiments with higher set of frequencies gave better performance of the system on the expense of slower reconstruction. [Figure 12\(a\)](#) shows the real image of the gauge blocks used in calibration process, [Fig 12\(b\)](#) shows the 3D point cloud height profile without texture, and [Fig12\(c\)](#) shows the 3D point cloud height profile with texture. [Figures 13\(a\)](#) and [\(c\)](#) show the real images of the Lincoln and lion statues, [Figs 13\(b\)](#) and [\(e\)](#) show the 3D point cloud height profile without texture, and [Figs 13\(c\)](#) and [\(f\)](#) show the 3D point cloud height profile with rendered texture.

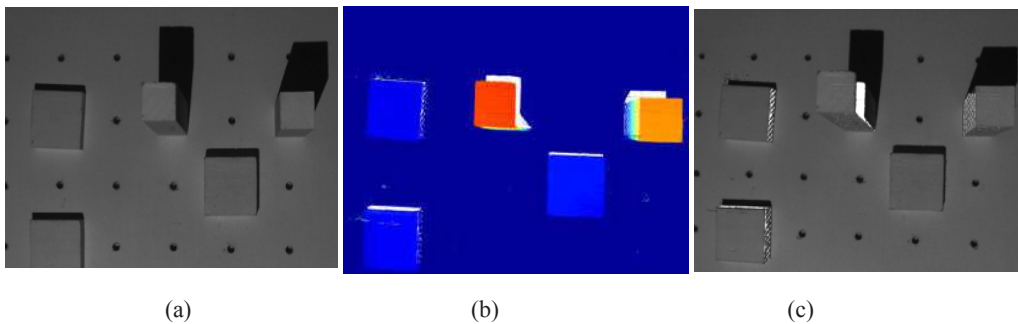


**Fig 12.** (a) Real image of the gauge blocks used in calibration process, (b) 3D point cloud height profile without texture, and (c) 3D point cloud height profile with texture.

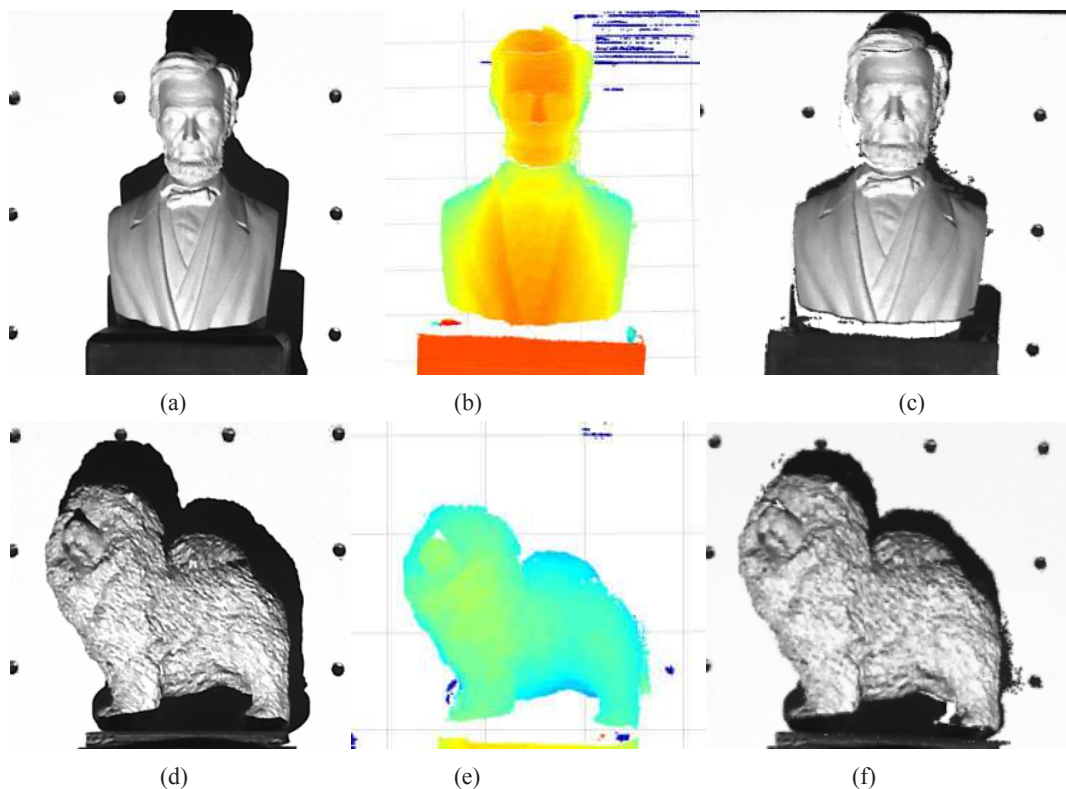


**Fig13.** 3D reconstruction of test objects: (a,d) Real images, (b,e) 3D point cloud height profile without texture, and (c,f) 3D point cloud height profile with rendered texture.

#### 4 MATLAB® based graphical user interface (GUI)

A MATLAB GUI was created to calibrate and control the fringe projection profilometry system. The interface allows users to directly change the inputs of the projected fringes such as: frequency, amplitude, the pattern of the fringe (horizontal or vertical), and number of fringe shifting steps. Also, the interface allows us to perform camera and system calibration, wrapped and unwrapped phase reconstruction, phase compensation, phase to height conversion, and texture rendering using 2D image registration. The final result will be a point cloud 3D image of the object. The process can be repeated automatically from different angles using a rotation stage controlled by Arduino through the GUI to acquire different point clouds from different perspectives.

A block diagram in Fig 14 gives a brief description of the operation of the MATLAB® interface (GUI). The interface is divided into two main parts: (a) Calibration part (Set-up) and (b) the Processing part. Firstly, the input parameters such as phase steps, amplitude modulation, fringe frequencies, and fringe orientation need to be set. In the second step, camera calibration using the checkerboard (See Fig 15(a)) is performed to obtain the intrinsic, extrinsic, and nonlinear distortion parameters followed by system calibration using calibration blocks with known dimensions to obtain the phase to height conversion parameters. This is shown in Fig 15(b). Also, in this step gamma correction is performed. After the calibration process is done, users don't need to calibrate the system again for 3D reconstruction of other objects unless the camera and/or the projector are moved.

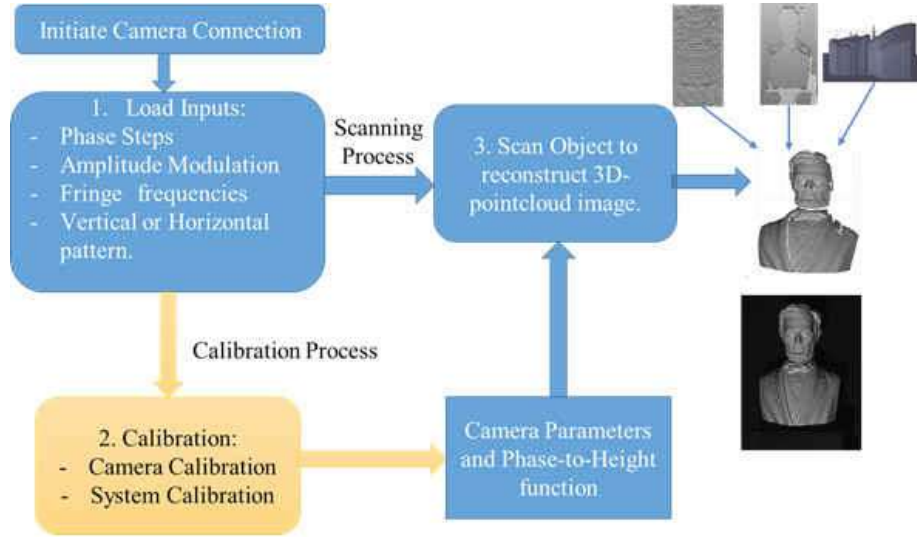


Fig 14. Detailed block Diagram of the GUI.

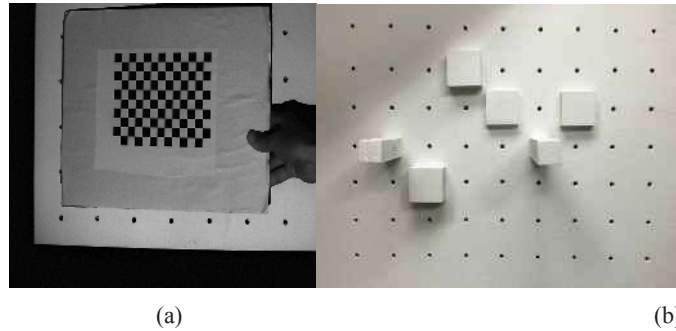


Fig 15. (a) The checker board used in camera calibration and (b) several cubes with varying dimension used in system calibration.

A graphical user interface (GUI) has also been developed to control, synchronize, and automate the whole process. A sample view of the GUI is shown in Fig 16. As in Fig 16, the interface gives the reconstruction result of the objects in various modalities for better visualization. The GUI computes the wrapped and unwrapped phases of the image and provides the depth information of the object as a depth image and simultaneously as a point cloud image. The interface is capable of merging point cloud images to create full 360 degrees 3-D point cloud image.

### 5 Image fusion using 3D registration

Iterative Closest Point (ICP) is an efficient and noise-resistant algorithm used to align partially overlapping point clouds to create a full view 3D object. Given two different point clouds, by using one as the reference  $\mathbf{P}_{\text{ref}}$  (fixed) and the other  $\mathbf{P}_{\text{mov}}$  as the source (moving), we can use ICP algorithm to find the translation and rotation matrices needed to align the two point clouds together through the minimization of the mean-square error (MSE).

The process is repeated until the error is sufficiently small. The algorithm is as follows:

- For each point in the source point cloud  $\mathbf{P}_{\text{mov}}$ , find the closest point in the reference point cloud

$$P_{\text{ref}} \min (1/M) \sum_{m=1}^M [v - \text{match } P_{\text{ref}}(v)]^2 \quad (30)$$

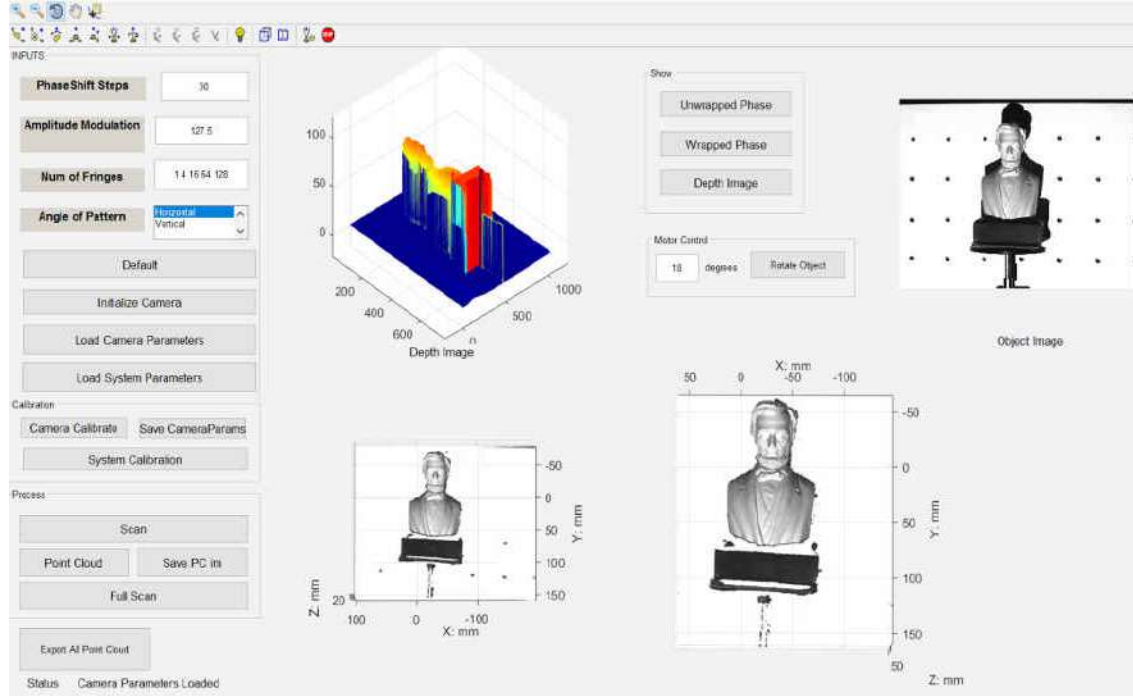


Fig 16. Developed graphical user interface (GUI) showing the Lincoln statue object.

The initial guess for the algorithm depends on the variation of the ICP method used. Some common choices are based on Euclidean distance, or curvature at a point, etc. The MSE function can be minimized by recursive algorithms such as gradient descent, Newton's method, conjugate gradient, or Levenberg-Marquardt algorithm [33].

(b) Reject outliers: Outliers are points that do not have a good corresponding point in the other point cloud, these points will negatively affect the result; therefore, they need to be removed first. To remove outliers, each matching pair will be assigned a weight based on the points' distances. Pairs whose weights satisfy a given condition will be discarded. The condition will vary depending on the algorithm used. Some algorithms set a fixed threshold for the weight while other may depend on the standard deviation.

(c) The algorithm will then try to estimate the best affine transformation  $\mathcal{S}$  (combination of rotation  $R$  and translation  $T$ ) to minimize the MSE cost function that will best align each source point to its match found in the previous step:

$$\min (1/M) \sum_{m=1}^M [\text{match}_{P_{\text{ref}}}(v) - (\mathcal{S} \times v)]^2 \quad (31)$$

The optimization method is the same as in the first step. The initial guess can be provided if additional information is available.

(d) Transform the source points using the obtained transformation:

$$P_{\text{ref}} = \mathcal{S} \times P_{\text{mov}}, \quad (32)$$

(e) Iterate: The above 4 steps will be repeated until the chosen error metric meets certain predefined condition. Both the error metric and the condition will vary based on the algorithm. After the algorithm

converges, the final result is the one that provides the best transformation matrix that will align the moving point cloud with the fixed point cloud.

The 3D scanning system outputs  $n$  different denoised point clouds  $P_k$ ,  $k = 1 \dots n$ , where consecutive point clouds are obtained from slightly different views. The full 3D point cloud model of the object can be obtained using the following equation

$$P = \cup_{k=1}^n A_k P_k = \cup_{k=1}^n (\prod_{i=1}^k S_i) P_k, \quad (33)$$

where  $P$  is the combined point cloud,  $P_k$  is the  $k^{\text{th}}$  point cloud,  $n$  is the total number of point clouds,  $A_k$  is the cumulative transformation matrix,  $S_i$  is the affine transformation matrix to align  $P_i$  with  $P_{i-1}$  when  $i > 1$ , and  $S_i$  is the identity matrix when  $i = 1$ . Typical full-field-of-view results for the Lion Statue object are shown in Fig 17.

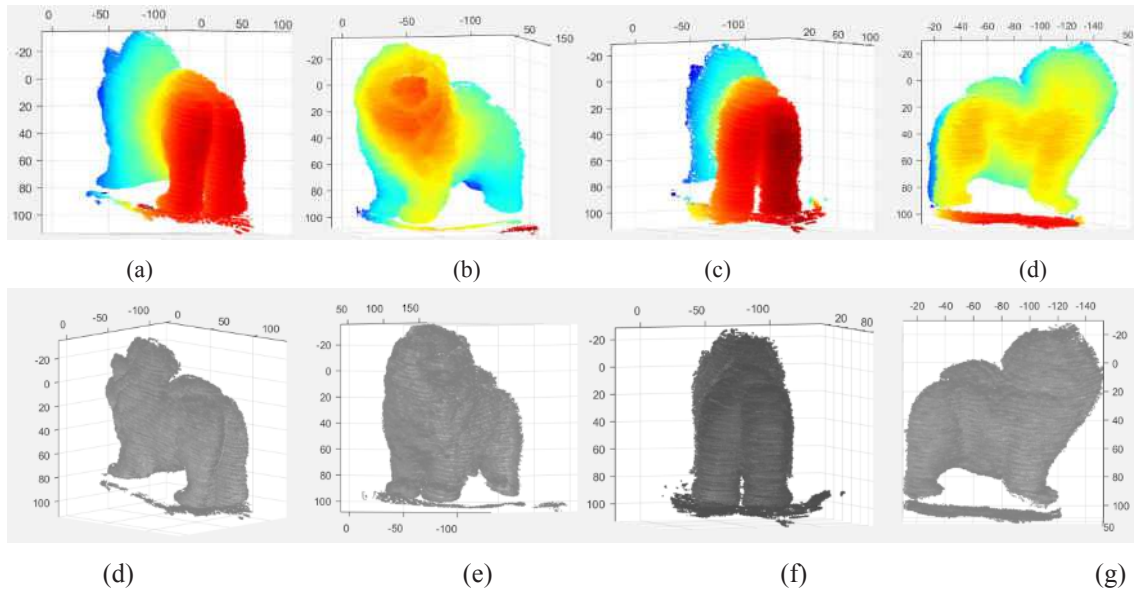


Fig 17. Full-field-of-view results using ICP algorithm: (a) 3D point clouds without texture and (b) 3D point clouds with texture.

## 6 Conclusion and Future Work

In this work, we constructed an automated, portable, tabletop, low cost, full field of view, 3D FPP scanning system from off-the-shelf components. A thorough comparative analysis of the various steps and techniques of a 3D imaging system based on FPP was conducted. Also, camera calibration, system calibration, several phase error compensation techniques, and phase unwrapping techniques, were discussed in details. Three-dimensional image fusion and point cloud registration was performed using an iterative closest point algorithm for a full field of view reconstruction. AMATLAB® based GUI was developed to control, automate, and synchronize the whole system. The GUI is equipped with different recording and reconstruction capabilities depending on the user's constraints of accuracy and speed. The experimental results at each step of the process were shown and the accuracy of the system was discussed. The FPP 3D imaging technology is still an area of active research due to all the advantages mentioned above. Future work will aim at increasing accuracy through the development of other nonlinear phase error compensation techniques. Finally, more robust and automatic image fusion techniques are currently under development.

## Appendix A

In this section, we explain how the initial guess for the camera parameters can be obtained. Equation (3) above relates the camera pixel coordinates to real world coordinates as in the following equation:

$$z_c \begin{bmatrix} u \\ v \\ 1 \end{bmatrix} = \begin{bmatrix} \alpha & \gamma & u_0 \\ 0 & \beta & v_0 \\ 0 & 0 & 1 \end{bmatrix} \begin{bmatrix} r_{11} & r_{12} & r_{13} & t_1 \\ r_{21} & r_{22} & r_{23} & t_2 \\ r_{31} & r_{32} & r_{33} & t_3 \end{bmatrix} \begin{bmatrix} x_w \\ y_w \\ z_w \\ 1 \end{bmatrix} \quad (\text{A.1})$$

which can be written in matrix format as:

$$z_c \begin{bmatrix} u \\ v \\ 1 \end{bmatrix} = \mathbf{K} \times [\mathbf{R}, \mathbf{T}] \begin{bmatrix} x_w \\ y_w \\ z_w \\ 1 \end{bmatrix} \quad (\text{A.2})$$

Multiplying the matrices of the intrinsic and extrinsic parameters, Eq (A.2) can be written as

$$z_c \begin{bmatrix} u \\ v \\ 1 \end{bmatrix} = \begin{bmatrix} q_{11} & q_{12} & q_{13} & q_{14} \\ q_{21} & q_{22} & q_{23} & q_{24} \\ q_{31} & q_{32} & q_{33} & q_{34} \end{bmatrix} \begin{bmatrix} x_w \\ y_w \\ z_w \\ 1 \end{bmatrix} \quad (\text{A.3})$$

Where  $\mathbf{Q} = \mathbf{K} \times [\mathbf{R}, \mathbf{T}]$ . Expanding Eq (A.3) we arrive at the following system of linear equations

$$\begin{cases} u = \frac{x_w q_{11} + y_w q_{12} + z_w q_{13} + q_{14}}{z_c} \\ v = \frac{x_w q_{21} + y_w q_{22} + z_w q_{23} + q_{24}}{z_c} \\ z_c = x_w q_{31} + y_w q_{32} + z_w q_{33} + q_{34} \end{cases} \quad (\text{A.4})$$

Notice that the unknowns are the twelve  $q_{ij}$  parameters. Measuring twelve pairs of  $u$ ,  $v$ ,  $x_w$ ,  $y_w$ , and  $z_w$ , Eq (A.3) can be written as:

$$\begin{bmatrix} x_{w_1} & y_{w_1} & z_{w_1} & 1 & 0 & 0 & 0 & 0 & -x_{w_1}u_1 & -y_{w_1}u_1 & -z_{w_1}u_1 & -u_1 \\ 0 & 0 & 0 & 0 & x_{w_1} & y_{w_1} & z_{w_1} & 1 & -x_{w_1}v_1 & -y_{w_1}v_1 & -z_{w_1}v_1 & -v_1 \\ \vdots & \vdots \\ x_{w_i} & y_{w_i} & z_{w_i} & 1 & 0 & 0 & 0 & 0 & -x_{w_i}u_i & -y_{w_i}u_i & -z_{w_i}u_i & -u_i \\ 0 & 0 & 0 & 0 & x_{w_i} & y_{w_i} & z_{w_i} & 1 & x_{w_i}v_i & -y_{w_i}v_i & -z_{w_i}v_i & -v_i \\ \vdots & \vdots \\ x_{w_{12}} & y_{w_{12}} & z_{w_{12}} & 1 & 0 & 0 & 0 & 0 & -x_{w_{12}}u_{12} & -y_{w_{12}}u_{12} & -z_{w_{12}}u_{12} & -u_{12} \\ 0 & 0 & 0 & 0 & x_{w_{12}} & y_{w_{12}} & z_{w_{12}} & 1 & -x_{w_{12}}v_{12} & -y_{w_{12}}v_{12} & -z_{w_{12}}v_{12} & -v_{12} \end{bmatrix} \begin{bmatrix} q_{11} \\ q_{12} \\ q_{13} \\ \vdots \\ \vdots \\ \vdots \\ \vdots \\ q_{34} \end{bmatrix} = 0 \quad (\text{A.5a})$$

Eq (A.5a) can be written in matrix format as

$$\mathbf{A}\mathbf{q} = 0, \quad (\text{A.5b})$$

where  $\mathbf{A}$  is a  $(24 \times 12)$  matrix, and  $\mathbf{q}$  is a  $(12 \times 1)$  linearized version of  $\mathbf{Q}$  matrix from Eq (A.3). The linear least square method is used to solve for the  $(24 \times 12)$   $\mathbf{q}$  matrix. The next step is to find the intrinsic and then the extrinsic parameters from the  $q_{ij}$  parameters. Let the matrix  $\mathbf{M}$  be defined as:

$$\mathbf{M} = \mathbf{K} \times \mathbf{R} = \begin{bmatrix} q_{11} & q_{12} & q_{13} \\ q_{21} & q_{22} & q_{23} \\ q_{31} & q_{32} & q_{33} \end{bmatrix} \quad (\text{A.6})$$

Let us define the matrix  $\mathbf{B} = \mathbf{M} \times \mathbf{M}^T$ . Since  $\mathbf{R}$  is an orthogonal matrix,  $\mathbf{R} \times \mathbf{R}^T = \mathbf{I}$ .  $\mathbf{B}$  can be written as

$$\mathbf{B} = \mathbf{K} \times \mathbf{R} \times \mathbf{R}^T \times \mathbf{K}^T = \mathbf{K} \times \mathbf{K}^T = \begin{bmatrix} \alpha^2 + \gamma^2 + u_0^2 & \gamma\beta + u_0v_0 & u_0 \\ \gamma\beta + u_0v_0 & \beta^2 + v_0^2 & v_0 \\ u_0 & v_0 & 1 \end{bmatrix} = \begin{bmatrix} b_{11} & b_{12} & b_{13} \\ b_{21} & b_{22} & b_{23} \\ b_{31} & b_{32} & b_{33} \end{bmatrix} \quad (\text{A.7})$$

Since the  $b_{ij}$  parameters are computed from the  $q_{ij}$  parameters, the intrinsic camera parameters are computed as follows:

$$\begin{cases} u_0 = b_{13}, \\ v_0 = b_{23}, \\ \beta = \sqrt{b_{22} - v_0^2} \\ \gamma = \frac{b_{12} - u_0v_0}{\beta} \\ \alpha = \sqrt{b_{11} - \gamma^2 - u_0^2} \end{cases} \quad (\text{A.8})$$

This means the intrinsic camera parameters defined in the  $\mathbf{K}$  matrix are computed. The following step is to find the reflection part of the extrinsic parameters from Eq (A.6):

$$\mathbf{R} = \mathbf{K}^{-1} \times \mathbf{M} \quad (\text{A.9})$$

The transmission part of the extrinsic parameters is found from Eq (A.3) using the following equation:

$$\mathbf{T} = \mathbf{K}^{-1} \times \begin{bmatrix} q_{14} \\ q_{24} \\ q_{34} \end{bmatrix} \quad (\text{A10})$$

## Appendix B

The following equations are derived to define the constants used in Eq (29) to compute the in-plane lateral coordinates  $x$  and  $y$  [17]:

$$p_1 = \frac{bx(u,v)cx(u,v) - ex(u,v)fx(u,v)}{gx(u,v)hx(u,v) - ix(u,v)jx(u,v)} \quad (\text{B1})$$

$$p_2 = \frac{ax(u,v)cx(u,v) - dx(u,v)fx(u,v)}{gx(u,v)hx(u,v) - ix(u,v)jx(u,v)} \quad (\text{B2})$$

$$p_3 = \frac{by(u,v)cx(u,v) - ey(u,v)fy(u,v)}{gy(u,v)hy(u,v) - iy(u,v)jy(u,v)} \quad (\text{B3})$$

$$p_4 = \frac{ay(u,v)cy(u,v) - dy(u,v)fy(u,v)}{gy(u,v)hy(u,v) - iy(u,v)jy(u,v)} \quad (\text{B4})$$

where

$$ax(u, v) = x_d r_{33} - r_{13}, ay(u, v) = ax(u, v) \quad (\text{B.5})$$

$$bx(u, v) = x_d t_3 - t_1, by(u, v) = bx(u, v) \quad (\text{B.6})$$

$$cx(u, v) = r_{22} - r_{32} y_{\text{cn}}, cy(u, v) = r_{21} - r_{31} y_{\text{cn}} \quad (\text{B.7})$$

$$dx(u, v) = y_d r_{33} - r_{23}, dy(u, v) = dx(u, v) \quad (\text{B.8})$$

$$ex(u, v) = y_d t_3 - t_2, ey(u, v) = ex(u, v) \quad (\text{B.9})$$

$$fx(u, v) = r_{12} - r_{32} x_{\text{cn}}, fy(u, v) = r_{11} - r_{31} x_{\text{cn}} \quad (\text{B.10})$$

$$gx(u, v) = r_{11} - r_{31} x_{\text{cn}}, gy(u, v) = r_{12} - r_{32} x_{\text{cn}} \quad (\text{B.11})$$

$$hx(u, v) = r_{22} - r_{32}y_{cn}, hy(u, v) = r_{21} - r_{31}y_{cn} \quad (B.12)$$

$$ix(u, v) = r_{21} - r_{31}y_{cn}, iy(u, v) = r_{22} - r_{32}y_{cn} \quad (B.13)$$

$$jx(u, v) = r_{12} - r_{32}x_{cn}, jy(u, v) = r_{11} - r_{31}x_{cn} \quad (B.14)$$

## References

1. Li L, Schemenauer N, Peng X, Zeng Y, Gu P, Robot, *Comp Integr Manuf*, 18(2002)53-67.
2. Rioux M, Blais F, *J Opt Soc Am*, 3(1986)1518-1521.
3. Godin G, Beraldin J A, Taylor J, Courmoyer L, Rioux M, El-Hakim S, Baribeau R, Blais F, Boulanger P, Domey J, Picard M, *IEEE Computer Graphics and Applications*, 22(2002)24-35.
4. Cheah C M, Chua C K, Tan K H, Teo C K, *Int J Prosthodont*, 16(2003)435-441.
5. Bouguet J Y, Perona P, In Proc Sixth Int Conf, Computer Vision, Bombay, India, (1998)43-48.
6. Baumberg A, Lyons A, Taylor R, *Graphical Models*, 67(2005)476-495.
7. Straub J, Kerlin S, *Proc SPIE*, Smart Biomedical and Physiological Sensor Technology XII, 9487(2015)94870X; doi: 10.1117/12.2176561.
8. Jarvis R A, *IEEE Trans Pattern Anal Mach Intell*, 5(1983)122-139.
9. Prince J, Real time 3D imaging for remote surveillance, US 8717418 B1.
10. Lamb R A, Hiskett P A, Wong G J, Gordon K J, Pawlikoska A M, Pilkington R, Sinclair P, *Proc SPIE*, Advanced Photon Counting Techniques VIII , 9114(2014); doi:10.1117/12.2051013
11. Thali M J, Braun M, Dirnhofer R, *Forensic Sci Int*, 137(2003)203-208.
12. Chen F, Brown G M, Song M, *Opt Eng*, 39(2000)10-22.
13. Sansoni G, Trebeschi M, Docchio F, *Sensors*, 9(2009)568-601.
14. Gorthi S S, Rastogi P, *Opt Lasers Eng*. 48(2010)133-140.
15. Feng S, Chen Q, Zuo C, Sun J, Yu S, In *Classical Optics 2014, OSA Technical Digest*, JTu5A(2014) JTU5A.42.
16. Zhang Z, *IEEE Transactions on Pattern Analysis and Machine Intelligence*, 22(2000)1330-1334.
17. Feng S, Chen Q, Zuo C, Sun J, Yu S L, *Opt Commun*, 329(2014)44-56; doi: doi:10.1016/j.optcom.2014.04.067
18. Zhang S, High-resolution, Real-time 3-D Shape Measurement, Ph D Dissertation Stony Brook University,(2005).
19. Lohry W, Zhang S, *Opt Lasers Eng*, 50(2012)917-921.
20. Minh V, Wang Z, Pan B, Pan T, *Opt Express*, 20(2012)16926-16941.
21. Zhang S, *Proc SPIE*, Dimensional Optical Metrology & Inspection for Practical Appl III, 9110(2014)911002.; doi:10.1117/12.2050534
22. Zhang S, Yau S-T, *Appl Opt*, 6(2007)36-43.
23. Zappa E, Busca G, *Opt Lasers in Eng*, 46(2008)106-116.
24. Nehmetallah G, Aylo R, Williams L, Analog and Digital Holography With MATLAB®, (SPIE Press, Bellingham, Washington), 2015.
25. Goldstein R M, Zebker H A, Werner C L, *Radio Sci*, 23(1988)713-720.
26. Navarro M A, Estrada J C, Servin M, Quiroga J A, *Opt Express*, 20(2012)2556-2561.
27. Zebker H A, Lu Y, *J Opt Soc Am A*, 15(1998)586-597.
28. Herráez M A, Burton D R, Lalor M J, Gdeisat M A, *Appl. Opt*, 41(2002)7437-7444.
29. Quan C, Tay C J, Chen L J, *Opt Laser Tech*, 39(2007)1155-1161.
30. Burke J, Bothe T, Osten W, Hess C, In Proc SPIE, Interferometry XI: Applications, 4778(2002)312; doi:10.1117/12.473547

31. Wang Z, Nguyen D A, Bames J C, *Opt Lasers Eng*, 48(2010)218-225.
32. Vo M, Wang Z, Hoang T, Nguyen D, *Opt Lett*, 35(2010)3192-3194.
33. Rusinkiewicz S, Levoy M, In Proc of the Third International Conference on 3-D Digital Imaging and Modelling, IEEE, (2001); doi: 10.1109/IM.2001.924423

[Received : 17.1.2017; accepted : 30.1.2017]

#### **Anh Thai**

Anh Thai is currently a Research Assistant and an MS student in the EECS department at CUA. She received her B.E.E degree in Electrical Engineering in 2015. Her areas of interest include 3-D imaging using fringe projection profilometry and computer vision. She is currently a student member of SPIE and OSA chapters at CUA.



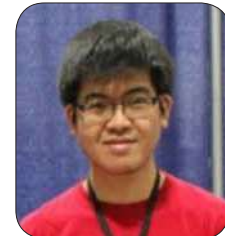
#### **Dat Tran**

Dat Tran is currently a Research Assistant and an MS student in the EECS department at CUA. He received his B.E.E degree in Electrical Engineering in 2016. His areas of interest include waveguide based spectrometry, 3-D imaging, and computer vision. He is currently a student member of SPIE and OSA chapters at CUA.



#### **Thanh Nguyen**

Thanh Nguyen is currently a Research Assistant and a Ph D student in the EECS department at CUA. He received his B.E.E degree and M.S degree in Electrical Engineering in 2012 and 2013, respectively. His areas of interest include 3-D imaging, digital holographic microscopy, transport of intensity imaging, and computer vision. Thanh received the SoE Millennium Scholarship since 2014. He is currently a student member of SPIE and the president of OSA chapter at CUA.



#### **George Nehmetallah**

Dr. George Nehmetallah is currently Assistant Professor in the EECS department at the CUA. From 2011-2012, he was at the University of Dayton (UD) as a Research Professor. Prior to this, he was a post-Doctoral Researcher and Research Engineer at UD where he received his PhD in 2006. He has served as a PI for several SBIR and STTR Phase I and Phase II projects from Air Force, Army, NASA, and DARPA and was one of the 11 out of over 500 that received the Army SBIR Achievement award in 2011. His research interests are in 3-D imaging, digital holography, and metamaterials. He has authored a book chapter on soliton stabilization, a book on analog and digital holography with MATLAB® and published more than 90 refereed journal papers, review articles, and conference proceedings. He is the recipient of the Newport Spectra-Physics Research Excellence Award(2005) and SPIE Educational Scholarship in Optical Science and Engineering (2005). He is a reviewer for Applied Optics, Optics express, Optics Letters and Asian J Phys. He is a senior member of OSA and SPIE.

